American Mineralogist, Volume 81, pages 229–237, 1996

Naturally occurring ferric iron sanidine from the Leucite Hills lamproite

SCOTT M. KUEHNER[1] AND DAVE J. JOSWIAK[2]

[1]Department of Geological Sciences, AJ-20, University of Washington, Seattle, Washington 98195, U.S.A.
[2]Department of Astronomy, FM-20, University of Washington, Seattle, Washington 98195, U.S.A.

ABSTRACT

Sanidine crystals precipitating from lamproitic magmas characteristically contain appreciable amounts of Fe^{3+}. Sanidine grains from the Leucite Hills lamproites (Wyoming) have compositions in which up to 70 mol% of the $KAlSi_3O_8$ molecule is replaced by $KFe^{3+}Si_3O_8$, thus constituting a new natural feldspar component.

Sanidine is among the last phases to crystallize in the groundmass of Leucite Hills lamproites and rarely exceeds 150 μm in length. Nearly all grains are zoned in Fe, ranging from 2.5 wt% Fe_2O_3 in the cores to 19.6 wt% Fe_2O_3 at rims adjacent to quenched glass. The Fe-rich rims are relatively narrow on (010) crystal faces in comparison with (001) faces (maximum width 10 μm), probably reflecting faster- (001) and slower-growing (010) crystallographic directions. A near-perfect correlation is obtained by combining Ti, Mg, and excess Si cations with Fe^{3+} in tetrahedral substitution for Al. Insufficient numbers of R^{2+} cations exist to balance the high concentrations of Mg through an $R^{2+}Mg^{2+}R^{1+}_{-1}R^{3+}_{-1}$ substitution, suggesting the exchange $Mg^{2+}Si^{4+}Al^{3+}_{-2}$ in $2KAlSi_3O_8$, analogous to that found in synthetic leucite and kalsilite. Selected-area electron diffraction and convergent-beam electron diffraction show that the Fe-rich sanidine rims have a $C2/m$ structure with cell dimensions of $a = 8.68 \pm 0.15$, $b = 13.14 \pm 0.23$, $c = 7.31 \pm 0.15$ Å, $\alpha = 90.0 \pm 0.54$, $\beta = 116.0 \pm 0.46$, $\gamma = 90.0 \pm 0.33°$, and a calculated cell volume of 747 ± 21 Å^3. These crystallographic data are in very close agreement to those obtained previously for synthetic $KFe^{3+}Si_3O_8$. The unusually high concentrations of Fe^{3+}, Ti, and Mg in the sanidine rims are likely the consequence of rapid crystallization during quenching of an unusually Si- and K-rich, yet Al-deficient residual magma.

INTRODUCTION

Smith (1974) and Smith and Brown (1988) reported that Fe is a ubiquitous minor element in both plagioclase and alkali feldspar. In alkali feldspars, a maximum of 4.8 wt% Fe_2O_3 was reported in sanidine grains in volcanic rocks from the Leucite Hills. Carmichael (1967) was the first to document the Fe-rich nature of sanidine found in the Leucite Hills lavas. Microprobe analyses of sanidine grains from seven different samples showed relatively high concentrations of Fe_2O_3 (2.7–4.8 wt%), corresponding to 10–18 mol% of the iron-sanidine component ($KFe^{3+}Si_3O_8$). Similar concentrations of Fe in sanidine were reported by Kuehner et al. (1981) and Gunter et al. (1990) from other Leucite Hills samples.

High-resolution, backscattered electron (BSE) imaging was not available for the studies of Carmichael (1967) and Kuehner et al. (1981). Using this method, however, we have found that nearly all sanidine grains in the samples studied display Fe zoning. Many of the sanidine grains have very Fe-rich rims with concentrations up to 19.6 wt% Fe_2O_3, corresponding to 70 mol% of the iron-sanidine component. End-member iron sanidine has been synthesized (Wones and Appleman 1961), but the natural feldspar end-member predominates only in sanidine from the Spanish Cancarix lamproite (up to 13.7 wt% Fe_2O_3; Linthout and Lustenhouwer 1993) and lamproites from the Leucite Hills. The Leucite Hills feldspars described here are the most Fe-rich, naturally occurring compositions yet recorded (Kuehner and Joswiak 1993).

GEOLOGICAL SETTING

The leucite-bearing volcanic rocks of the Leucite Hills were first described by Emmons (1877) and include 30–40 flows ranging in thickness from 20 cm to 38 m (Ogden 1979). K-Ar dates from five of the volcanic centers range from 1.1 to 3.1 Ma (Bradley 1964; McDowell 1971; Mitchell and Bergman 1991). The volcanic rocks are lamproites, which are defined as having whole-rock molar $K_2O/Na_2O > 3$, $K_2O/Al_2O_3 > 1$, $K_2O > 5$ wt%, and MgO > 5 wt% (see review by Mitchell and Bergman 1991). Typically, lamproites have high Fe_2O_3/FeO molar ratios. The Leucite Hills samples have molar Fe_2O_3/FeO ratios from 0.5 to 3.3, with 25 of 30 published analyses having ratios greater than 1 (Cross 1897; Yagi and Matsumoto 1966; Carmichael 1967; Barton and Hamilton 1978, 1982; Kuehner et al. 1981; Gunter et al. 1990).

Three volcanic rock types, defined mainly on the basis of mineralogy, occur in the Leucite Hills: orendite,

0003–004X/96/0102–0229$05.00

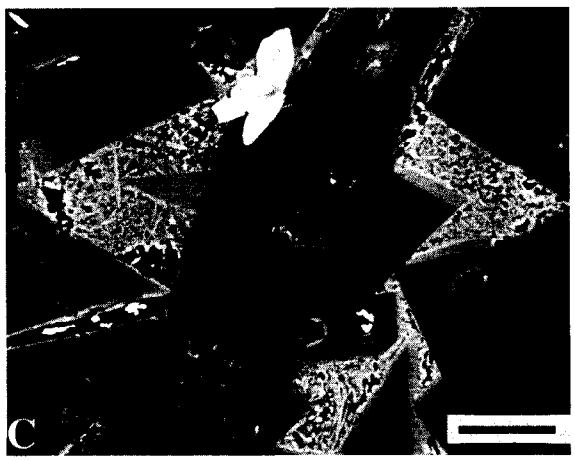

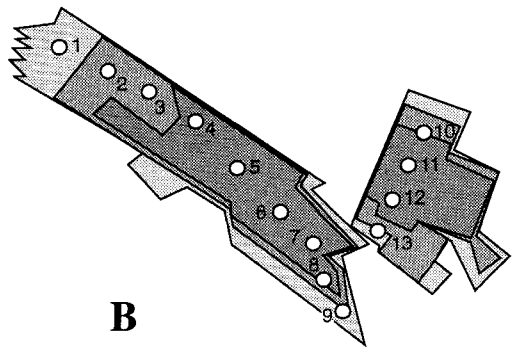

FIGURE 1. (A) Backscattered electron (BSE) image of the groundmass assemblage of sample LH37. Blocky, euhedral crystals of sanidine with bright Fe-rich rims in a groundmass of glass and quenched crystallites. Large bright grains are apatite; irregular rounded grains are leucite (medium gray), which may be partially replaced by analcime (dark). A grain of Ti- and K-rich richterite (bottom center) partially encloses leucite, whereas other Ti- and K-rich richterite grains are interstitial to sanidine (upper left). Scale bar is 100 μm. (B) Sketch of two strongly zoned sanidine grains (see A) analyzed by microprobe. The indicated points correspond to the analyses in Table 1. (C) Blocky sanidine grains with bright Fe-rich rims in fresh glass. The glass has numerous crystallites of an unidentified mineral. The large bright grains are apatite, the very small, irregular bright grains are Sr-rich barite. Scale bar is 20 μm.

wyomingite, and madupite (Cross 1897). Orendite corresponds to diopside + sanidine + phlogopite lamproite of Mitchell and Bergman (1991). Sanidine is the predominant groundmass phase in these rocks, with smaller amounts of leucite and Ti- and K-rich richterite. Wyomingite is similar but has a groundmass composed mainly of leucite. Both rock types have phenocrysts of phlogopite, diopside, and apatite. Madupite has phenocrysts of diopside with large irregular patches of groundmass phlogopite poikiliticly enclosing diopside, apatite, perovskite, and leucite. Accessory phases in these rocks include forsteritic olivine, wadeite [$K_4Zr_2Si_6O_{18}$], priderite [$(K,Ba)(Ti,Fe^{3+})_8O_{16}$], and Sr-rich barite.

PARAGENESIS

All the volcanic rocks in the Leucite Hills are very fine grained. Phlogopite phenocrysts and rare xenocrystic olivine and orthopyroxene are the only macroscopic phases. They are typically 1–2 mm in length, though in some cases they may reach 4 mm. Sanidine crystals are among the last phases to crystallize in orendite (Fig. 1). Individual sanidine grains, typically <150 μm long, may reach 400 μm in length in coarse-grained samples. The sanidine grains often enclose small grains of olivine, apatite, and diopside but only rarely enclose portions of leucite and Ti- and K-rich richterite. Carmichael (1967) reported from an optical determination that the crystals have high-sanidine structure. The sanidine grains are elongated parallel to the c axis (finisterre habit), resulting in trapezoidal shapes in sections paralleling (010) and rectangular shapes in sections broadly perpendicular to (010). The crystals show prominent (100), (010), and ($\bar{1}$01) faces. The {001} form has not been recognized. Carlsbad twinning is common.

Nearly all sanidine grains display a rimward increase in Fe as indicated by the increasing gray-scale brightness in BSE images (Fig. 1). However, only those grains adjacent to angular interstices have the visually pronounced, bright Fe-rich rims; the extreme Fe enrichment is not observed at sanidine grain edges that are bound by other crystalline phases. The Fe-rich rims are relatively narrow on faces in the [001] zone, whereas they are well developed on crystal faces broadly perpendicular to the [001] zone axis where the rims may reach 10 μm in thickness. The very small size of the Fe-rich sanidine rims precludes any optical and conventional X-ray diffraction characterization.

Figures 1A and 1B show that the Fe-rich rim of one sanidine grain is interdigitated with the interstitial material, whereas other examples show extensions of rims intergrown with the interstitial material in a graphiclike texture. The interstitial material commonly contains bright (in BSE), randomly oriented, stout to acicular phases (Fig. 1C). Thus, the interstitial material is probably a mixture of glass and acicular quenched crystallites. Defocused beam analyses of the interstitial material (Table 1) show very high concentrations of Zr, Ti, Ba, and Sr, consistent with a late-stage liquid. Unidentified secondary minerals also occur in interstitial voids but are easily distinguished from magmatic phases by their concentric chemical zoning (Fig. 1A). Despite the occurrence of some secondary material, the presence of unaltered leucite in the extrusive facies of the Leucite Hills volcanics shows that these rocks are very fresh in comparison with rocks from other North American lamproite localities (Smokey Butte, Montana, Mitchell et al. 1987; Francis, Utah, Best et al. 1968), which excludes the possibility that the Fe-rich sanidine rims could have formed during a subsolidus alteration episode (Gupta and Fyfe 1975).

TABLE 1. Typical orendite whole-rock analysis and interstitial glass composition

	LH35* Whole rock	LH37 Avg. glass	Glass range	CIPW Norm	LH35 Whole rock	LH37 Avg. glass
SiO_2	54.86	51.2	45.0–57.0	Q	0.3	28.4
TiO_2	2.52	6.33	3.02–8.73	zr	0.2	6.3
Al_2O_3	10.80	2.56	1.80–3.82	ap	3.0	1.2
Cr_2O_3	0.06	n.d.		ilm	2.0	13.4
Fe_2O_3	3.00	n.d.		or	58.9	15.3
FeO	0.96	7.84**	6.45–9.96	ks	1.3	21.4
MnO	0.05	n.d.		ns		0.1
MgO	6.56	2.44	1.24–4.04	ac	6.9	
CaO	3.57	1.42	0.42–2.07	di	4.6	4.3
SrO	0.20	0.09	0.05–0.13	hyp	14.3	8.6
BaO	0.52	0.46	0.02–0.93	hm	0.6	
Na_2O	1.24	0.24	0.06–0.64	cr	0.2	
K_2O	10.70	14.4	12.3–17.2	tn	3.7	
P_2O_5	1.32	0.51	0.12–0.94	th	0.7	
SO_3	0.37	<mdl				
ZrO_2	0.18	3.88	3.30–5.07			
Cl	n.d.	<mdl				
F	n.d.	<mdl				
LOI	3.24					
Total	100.15	91.4	83.3–98.1			

Note: Whole-rock analyses by XRF, Fe^{3+}/Fe^{2+} by titration; glass analyses by microprobe; n.d. = not determined; <mdl = less than minimum detection limit (weight percent; Reed 1973): Cl 0.012, F 0.04; SO_3 0.05.

* North Table Mountain sample LH35 (Kuehner et al. 1981); LH37 whole rock was not analyzed.

** Total Fe as FeO; number of analyses = 6.

METHODS OF CHEMICAL ANALYSIS

Wavelength-dispersive analyses of the sanidine grains and glass were obtained using a JEOL JXA733 electron microprobe with Tracor Northern software. Peak counting times were 24–25 s for Si (0.5% precision) and 40 s for all other elements. A variety of analytical conditions were evaluated to eliminate beam-induced element mobility and still permit acquisition of zoning profiles for the small sanidine grains. At 15 kV, 5 nA, and a 3 μm beam diameter, there was found to be no significant variation in the count rates over a 40 s time period. Si, Al, K, and Fe peak counts were all acquired during the first 40 s of beam exposure to the sample.

Although the feldspars in four orendite samples were examined using BSE imaging, only those in Spring Butte sample SK37 were analyzed. Core-rim zoning profiles were obtained from two sanidine grains (Fig. 1B; Table 2). The remaining analyses were from randomly selected grains. To determine how close to crystal edges analyses could be obtained without fluorescing adjacent glass, Zr counts were collected in 3 μm steps across a rim and into adjacent glass (3.9 wt% ZrO_2). Apparent Zr concentrations were below the detection limit (<0.03 wt% ZrO_2) when analyses were more than 3 μm from the crystal-glass boundary. The high concentrations of Fe and Ti found in the sanidine rims were also independently confirmed by energy-dispersive analysis (EDS) by transmission electron microscope (TEM).

MICROPROBE RESULTS

Microprobe analyses of the Leucite Hills feldspar (Table 2) show that the molar 100K/(K + Na + Ca) ratio ranges from 95 to 97, corresponding to K-sanidine on the basis of the definition of Smith and Brown (1988). In addition to a broad range of Fe_2O_3 concentrations (2.2–18.9 wt%) and corresponding inverse variation in Al_2O_3 (16.8–2.6 wt%), analyses of the sanidine grains show appreciable amounts of TiO_2 (0.2–1.1 wt%) and MgO (0.1–0.7 wt%). The Leucite Hills sanidine has up to ten times the previously reported maximum concentration of TiO_2 in a potassium feldspar (Smith and Brown 1988). Linthout and Lustenhouwer (1993) did not analyze TiO_2 content in the Fe-rich rims, but they reported up to 0.46 wt% MgO in the Cancarix sanidine. The MgO concentration in the Fe-rich rims of Leucite Hills sanidine also exceeds that found in the sanidine described by Smith and Franks (0.53 wt%; 1986).

Substitution of Fe^{3+} into $KAlSi_3O_8$ is expected to follow the exchange $Fe^{3+}Al_{-1}$ (Annersten 1976; Petrov and Hafner 1988). However, Figure 2 shows that as Fe^{3+} increases, there is increasing deficiency in Fe^{3+} compared with the ideal 1:1 relationship, suggesting that other cations are also filling T sites. Other cations possibly participating in Al substitutions on the T site are Ti, Mg, and Si. A plot of Si vs. Al (not shown, but see Table 2) indicates that for Al-rich compositions Si tends to be <3.00 cations, whereas for Al-poor compositions Si tends to be >3.00 cations. This suggests that at low values of Al, excess Si cations plus a divalent cation may be substituting for Al ($R^{2+}SiAl_{-2}$). A plot of Al vs. [(Si − 3.00) + Ti + Mg + Fe] (Fig. 2) shows a nearly perfect 1:1 relationship, suggesting that the unusually high concentrations of Ti, Mg, and Fe^{3+} can be accommodated stoichiometrically in sanidine by substituting for $^{[4]}Al$.

TABLE 2. Microprobe analyses of sanidine

Analyses*	1	2	3	4	5	6	7	8	9	10	11	12	13
						wt% oxides							
SiO_2	60.0	63.2	62.7	63.8	63.7	63.5	62.6	61.8	59.6	62.8	64.3	63.6	63.9
TiO_2	0.68	0.24	0.25	0.29	0.34	0.38	0.38	0.48	1.44	0.49	0.31	0.30	0.31
Al_2O_3	3.36	12.2	13.9	16.5	16.3	15.8	15.7	9.46	2.56	9.15	16.1	16.4	15.3
Fe_2O_3**	18.4	7.55	5.27	2.54	2.86	2.96	3.20	10.3	18.1	10.7	2.84	2.38	3.80
MgO	0.65	0.39	0.40	0.16	0.18	0.59	0.19	0.53	0.71	0.51	0.18	0.16	0.35
CaO	<mdl	<mdl	0.07	0.02	0.03	0.14	0.13	0.10	0.06	0.03	<mdl	0.03	0.09
Na_2O	0.36	0.33	0.33	0.33	0.30	0.27	0.32	0.34	0.32	0.31	0.34	0.43	0.30
K_2O	14.9	15.6	15.4	16.2	16.0	15.7	16.1	15.6	15.3	15.9	15.8	16.2	15.8
BaO	0.24	0.37	0.66	0.78	0.59	0.72	0.62	0.39	0.15	0.46	0.56	0.68	0.71
SrO	<mdl	0.10	0.05	0.07	<mdl	0.05	<mdl	0.07	0.07	0.05	0.04	0.06	0.13
Total	98.7	99.98	99.0	100.7	100.3	100.1	99.2	99.1	98.3	100.4	100.5	100.2	100.7
						Cations calculated on the basis of 8 O atoms							
Si	3.025	3.011	2.996	2.979	2.980	2.980	2.975	3.014	3.021	3.026	3.000	2.979	2.990
Ti	0.026	0.009	0.009	0.010	0.012	0.014	0.012	0.018	0.055	0.018	0.011	0.010	0.011
Al	0.200	0.685	0.783	0.908	0.900	0.874	0.879	0.543	0.160	0.520	0.880	0.909	0.844
Fe^{3+}	0.698	0.270	0.190	0.089	0.101	0.105	0.115	0.378	0.691	0.388	0.100	0.084	0.134
Mg	0.049	0.028	0.028	0.011	0.012	0.042	0.014	0.038	0.053	0.036	0.012	0.011	0.025
Ca	0	0	0.003	0.001	0.001	0.007	0.007	0.005	0.003	0.002	0	0.002	0.005
Na	0.035	0.031	0.030	0.030	0.027	0.025	0.029	0.032	0.032	0.029	0.031	0.039	0.027
K	0.959	0.948	0.940	0.965	0.955	0.940	0.976	0.971	0.990	0.977	0.940	0.968	0.943
Ba	0.005	0.007	0.012	0.014	0.011	0.013	0.012	0.007	0.003	0.009	0.010	0.013	0.013
Sr	0	0.003	0.001	0.002	0	0.001	0	0.002	0.002	0.001	0.001	0.002	0.003
Total	4.997	4.992	4.992	5.009	4.999	5.001	5.019	5.008	5.010	5.006	4.985	5.017	4.995

Note: <mdl = less than minimum detection limit (weight percent; Reed 1973): Na_2O 0.02, MgO 0.02, CaO 0.03, TiO_2 0.04, SrO 0.06, ZrO_2 0.03, BaO 0.08.

* Analyses correspond to the points indicated in Figure 1B.

** Total Fe reported as Fe_2O_3.

ELECTRON DIFFRACTION

An electron diffraction study was conducted to confirm that the Fe-rich rims of the sanidine grains had the feldspar structure. Because of the small size of the Fe-rich rims, conventional X-ray diffraction was not possible.

Methods

A cluster of several sanidine grains, each with approximately 10 μm wide Fe-rich rims, was located with BSE imaging on a standard thin section. A high-speed dental drill was used to remove a 100 μm square fragment containing these grains. The fragment was mounted in an epoxy bullet and microtomed into several ~1000 Å slices, which were collected onto a 3 mm copper TEM grid previously coated with a carbon substrate. Because the sanidine grains shattered during microtoming, the iron-sanidine rim fragments were first identified in STEM mode using the EDS detector.

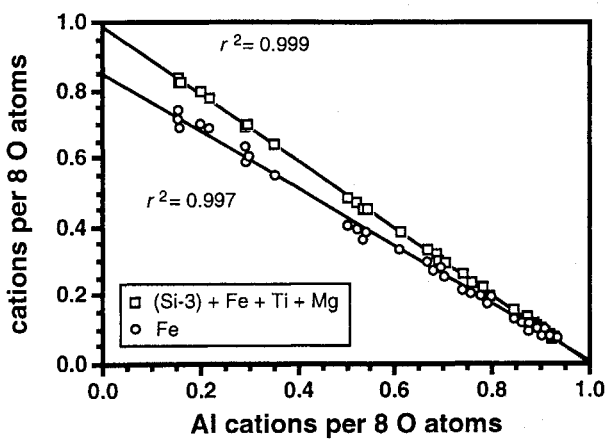

FIGURE 2. Cation plot of Al substitution in sanidine. Circles show that there is a progressive tetrahedral site deficiency for the exchange $FeAl_{-1}$. Only by including nonstoichiometric Si + Ti + Mg with Fe is the 1:1 substitution for Al preserved (squares).

Selected-area electron diffraction (SAED) patterns were obtained with a JEOL JEM-1200EX TEM operating at 120 kV using a tilt-rotate sample holder. The TEM was equipped with a GATAN 622 SC imaging system and a Tracor Northern 5500 EDS X-ray analysis system. All SAED patterns were recorded at a camera length of 200 mm using a 20 μm condenser-lens aperture after first focusing the electron diffraction image on the back focal plane of the objective lens. The camera length was calibrated using an evaporated thin-film aluminum standard. A Scion LG-3 frame-grabber board was used to import 40 of the SAED patterns from the TEM into a Centris 650 Macintosh computer, which measured the patterns using NIH Image version 1.53 (see Acknowledgments section) and indexed them by comparison with the 1989 powder diffraction file for synthetic sanidine of the Joint Committee for Powder Diffraction Standards, International Center for Diffraction Data. Each of our acquired patterns showed internal consistency between the measured angles for all combinations of (*hkl*) planes. Angle and *d* measurements from [200], [020], and [001] zone-axis patterns were obtained from digitized negatives of

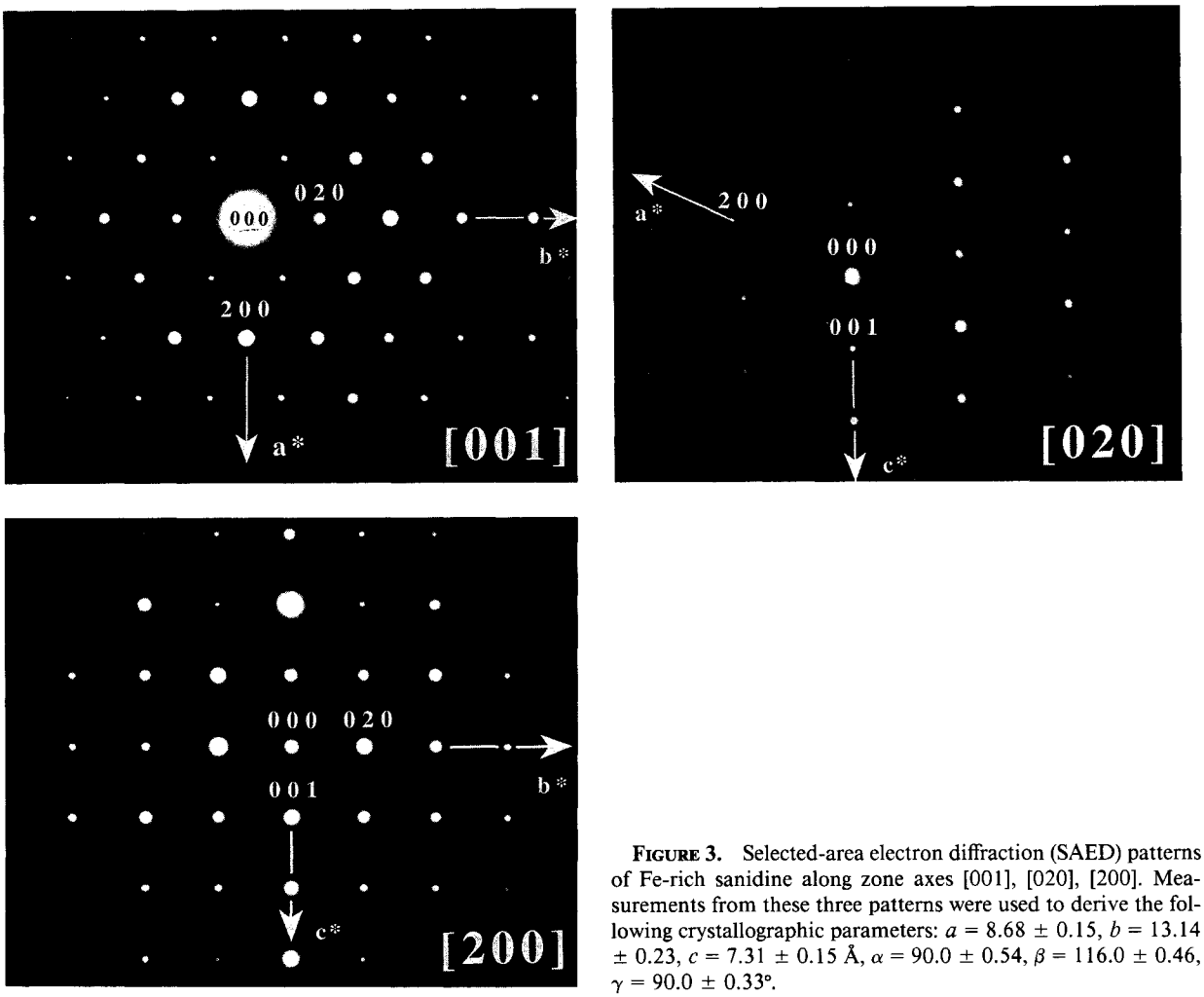

FIGURE 3. Selected-area electron diffraction (SAED) patterns of Fe-rich sanidine along zone axes [001], [020], [200]. Measurements from these three patterns were used to derive the following crystallographic parameters: $a = 8.68 \pm 0.15$, $b = 13.14 \pm 0.23$, $c = 7.31 \pm 0.15$ Å, $\alpha = 90.0 \pm 0.54$, $\beta = 116.0 \pm 0.46$, $\gamma = 90.0 \pm 0.33°$.

SAED patterns using the NIH Image program to determine the center of each reciprocal lattice diffraction spot and Microsoft Excel to calculate the d and angles. Angles were determined from least-squares regression lines drawn through spot centers of the appropriate row and column pairs. The procedure was calibrated with a [100] zone-axis pattern from fluorite (measured angle = 90.1 ± 0.4°) obtained under the same analytical conditions as the iron-sanidine patterns. Eleven of the d values of the iron sanidine were measured from diffraction patterns recorded on film and projected onto a microfilm viewing screen. The carbon-film substrate on the TEM grid was used as an internal standard to calibrate the projection.

Convergent-beam electron diffraction (CBED) patterns were recorded on film from a Phillips 430T TEM operating at 100 kV using a double-tilt holder and condenser-lens apertures of 100 and 200 μm. For indexing purposes, SAED patterns were recorded on film in conjunction with the CBED patterns. An evaporated, thin-film aluminum standard was used for camera-length calibration.

Electron diffraction results

Figure 3 shows the SAED patterns along crystallographic axes a, b, and c, each obtained from separate iron-sanidine rim fragments. Indexing of the patterns reveals systematic absences in the a^* and b^* directions ($h + k$ = even), indicating a C-face–centered cell with crystallographic axes corresponding to the zone axes [200], [020], and [001], respectively. Angle and d measurements taken from these patterns are given in Table 3. Although inherently much less precise, the electron diffraction results are in very good agreement with the X-ray powder diffraction data of synthetic monoclinic iron sanidine (Table 3). Linthout and Lustenhouwer (1993) reported X-ray diffraction data from Cancarix sanidine, but their measurements were from a mixture containing Fe-rich rims and Fe-poor cores. Thus, their more precise measurements do not correspond to the Fe-rich rim compositions.

To determine the unique point group for monoclinic iron sanidine, two whole-pattern (WP) CBED patterns were

TABLE 3. Iron-sanidine cell dimensions from SAED patterns

	a (Å)	*b* (Å)	*c* (Å)	α (°)	β (°)	γ (°)
[200]		13.15		90.0		
Error*		(0.28)		(0.54)		
*n***		58		63		
[020]	8.68		7.31		116.0	
Error	(0.15)		(0.15)		(0.46)	
n	47		33		39	
[001]		13.12				90.0
Error		(0.37)				(0.33)
n		63				46
Avg.	8.68	13.14	7.31	90.0	116.0	90.0
Error	(0.15)	(0.23)	(0.15)	(0.54)	(0.46)	(0.33)
W-A†	8.68	13.12	7.31		116.1	
Error	(0.01)	(0.02)	(0.01)		(0.083)	

* One standard deviation in *d* measurements between adjacent diffraction disks or the standard deviation in angle measurements between row-column pairs.

** The number of diffraction disk pairs or row-column angles measured.

† Wones and Appleman (1961).

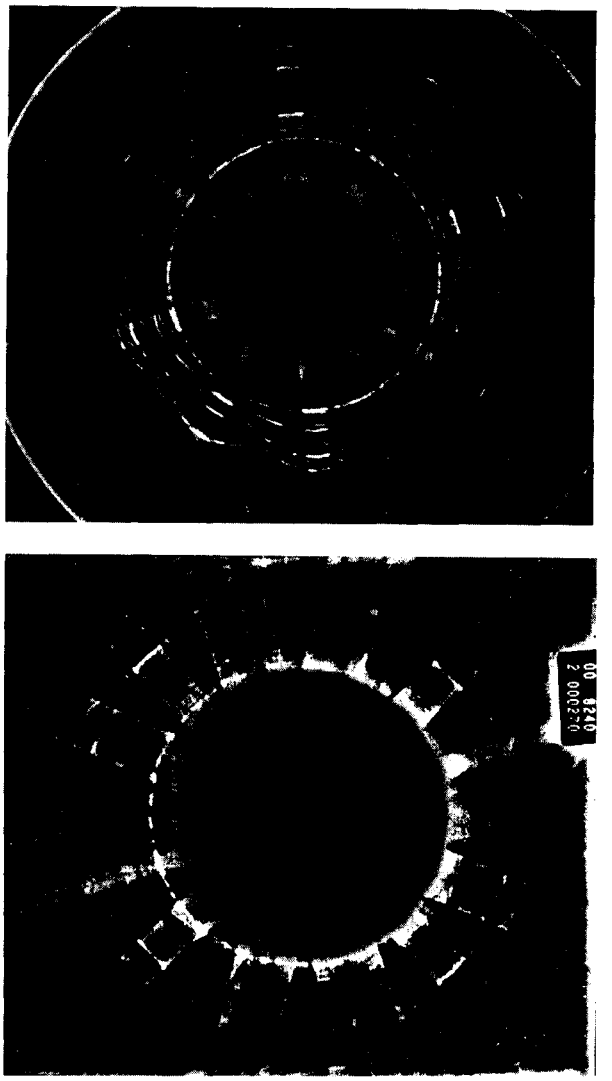

FIGURE 4. (**A**) Convergent-beam electron diffraction (CBED) pattern of iron sanidine along zone axis [001] showing a mirror line along a NE-SW axis (arrows). (**B**) CBED pattern of iron sanidine along zone axis [020] showing a single twofold axis. Both of the original CBED photographic negatives were digitized and their features enhanced using the high pass filter in Adobe Photoshop.

obtained along the zone axes [001] and [020] (Fig. 4) at a camera length of 270 mm. Examination of the WP symmetry of [001] shows a single mirror line, whereas the WP symmetry of [020] has a twofold axis. Following the method of Champness (1987) and the knowledge from the SAED patterns that the unit cell is monoclinic, the CBED zone-axis patterns show that the unique point group for the naturally occurring Leucite Hills iron sanidine is $2/m$.

DISCUSSION

To evaluate charge balance and stoichiometry on the basis of tetrahedrally coordinated Si, Ti, Al, Fe^{3+}, and Mg, the following feldspar components were calculated: $CaMgSi_3O_8$, $(Ba,Sr)Al_2Si_2O_8$, $NaAlSi_3O_8$, $KAlTi_3O_8$, $KFe^{3+}Si_3O_8$, and $KAlSi_3O_8$. Ca was treated separately from other divalent cations (Ba, Sr) because a $CaMgSi_3O_8$ feldspar has been synthesized (Sclar and Benimoff 1980) and because the occurrence of this component has been reported in both synthetic plagioclase crystals (Tsuchiyama 1985) and natural sector-zoned plagioclase crystals from glassy submarine basalts (Bryan 1974). The calculations show, however, that there is insufficient Ca to balance Mg in a $CaMgR^{1+}_{-1}R^{3+}_{-1}$ substitution. Even if Ba were combined with Ca, there would still be a deficiency in the number of R^{2+} cations needed to charge balance Mg. Ba, however, decreases with increasing Mg, indicating that Ba is not charge coupled to Mg. Sr concentrations are near the detection limit of the analytical method and are thus insignificant. This suggests that Mg may exist as the A-site vacant, negatively charged feldspar molecule $(\square MgSi_3O_8)^{2-}$, or that the charge imbalance resulting from $^{[4]}Mg$ substitution is compensated by A-site K^+.

From the chemistry alone, we are unable to determine uniquely which of these two choices may be correct. If, however, the charge imbalance is compensated by A-site K^+, it would indicate the occurrence of the charge-balanced component $K_2(MgSi)Si_6O_{16}$ through the substitution of $MgSiAl_{-2}$ in $2KAlSi_3O_8$. The $K_2(MgSi)Si_6O_{16}$ component can be considered the sum of the charge-imbalanced feldspar components $(KMgSi_3O_8)^-$ and $(KSi-Si_3O_8)^+$. Although a feldspar of $K_2MgSi_7O_{16}$ composition has not been experimentally produced, such a molecule has previously been proposed as a significant component in a natural Mg-rich sanidine (Smith and Franks 1986). Analogous isomorphic polymorphs of kalsilite ($K_2MgSi_3O_8$) and leucite ($K_2MgSi_5O_{12}$), however, have been synthesized, and in the case of $K_2MgSi_5O_{12}$, experimental evidence shows that it forms a continuous solid-solution series with leucite (Schairer 1948; Roedder 1951). Although this does not prove the existence of a $K_2MgSi_7O_{16}$-sanidine solution series, such a molecule does

satisfy the R_5O_8 stoichiometry and charge-balance requirements for feldspar. A maximum of 5.4 mol% of the $K_2MgSi_7O_{16}$ molecule is calculated from analyses of the Leucite Hills sanidine grains. Alternatively, a maximum of 4.9 mol% of the $\square MgSi_3O_8$ molecule is calculated.

Regardless of the choice of magnesium feldspar component, in many cases there remains an excess of Si and K atoms following calculation of the feldspar molecules. When plotted (Fig. 5), the K and Si excesses define a trend of approximately 1K:2Si ($R^2 = 0.81$). Similarly correlated excesses of K and Si are also found in the Fe-rich sanidine grains from Cancarix (Linthout and Lustenhouwer 1993). The correlation of these excess components implies that the nonstoichiometric cation surpluses are not randomly incorporated into the M and T sites in growing sanidine grains but are coupled either in single components such as $K_2Si_4O_9$ or $K\square(\square Si_2)O_8^{7-}$ or, alternatively, are incorporated as two separate components, the proportions of which are externally controlled. On the basis of published simple-system experiments, Linthout and Lustenhouwer (1993) suggested that the excess K and Si found in the Cancarix iron sanidine resulted from solid solution of potassium tetrasilicate and silica in sanidine during eutectic crystallization.

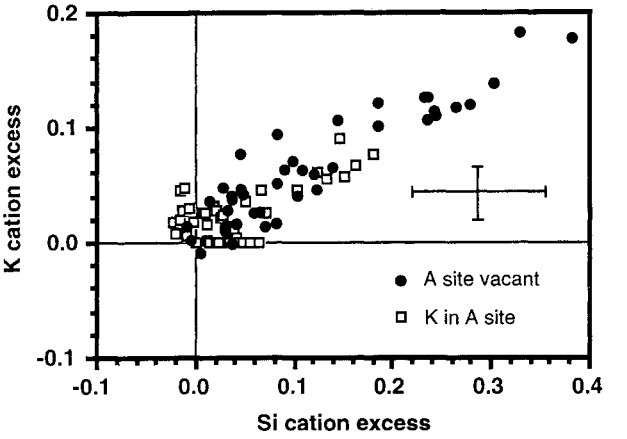

FIGURE 5. Excess cations of Si and K, following calculation of feldspar components (see text), define a trend of approximately 1K:2Si. Results from both magnesium feldspar component calculations are shown: circles for $\square MgSi_3O_8$, squares for $K_2MgSi_7O_{16}$. The error bar represents the largest $\pm 1\sigma$ analytical error propagated through the feldspar component calculations following Bevington (1969).

CRYSTALLIZATION TRENDS

Figure 6 shows that the concentrations of Mg and Ti increased in sanidine as crystallization progressed, Ba decreased, and Na remained constant. With the exception of Na, the concentration of each minor element displays a prominent change in slope at about 8 wt% Fe_2O_3, which coincides with the sharp transition from dark gray to light gray on the BSE images. A qualitative interpretation of the zoning patterns is possible by noting that magmatic phases generally display a progression of crystal shapes from equant tabular through acicular skeletal to spherulitic with increasing degrees of supercooling (Lofgren 1980). The empirical observation that the finisterre habit of sanidine is typical of volcanic rocks has been used as evidence to indicate that this feldspar growth form is the result of relatively rapid cooling (Smith 1974; Woensdregt 1983; Smith and Brown 1988), and the fingerlike projections of Fe-rich rim material on some Leucite Hills sanidine grains is evidence of even more rapid crystal growth during the final stages of crystallization (Fig. 1) in these samples.

Theoretical and experimental studies have shown that crystal-liquid partitioning of trace elements is strongly related to crystal growth rates (Albarede and Bottinga 1972; Grove and Bence 1977; Lofgren 1980; Shimizu 1983; Kuehner et al. 1989). If the crystal growth rate is comparatively rapid, the liquid boundary layer at the crystal interface becomes enriched with incompatible trace elements and depleted in compatible trace elements relative to the bulk liquid. The resulting concentration profile for a particular element depends, in part, on the crystal growth rate and the diffusion coefficient for that element in the liquid. Petrographic evidence suggests that trace element–rich boundary layers were present during the final stages of crystallization in sample LH37. Figure 7 is an image of an interstitial glass region between sanidine grains. Planar Fe-rich sanidine rims have ragged overgrowths of even more Fe-rich (on the basis of gray scale brightness) rim material projecting into the glass. Separating the ragged projections from the glass are very narrow (<2 μm), bright coatings. Although the coatings are too small for microprobe analysis, their EDS spectra and relative brightness in the BSE image indicate that the coatings are rich in high atomic-number elements Ti, Zr, Sr, and REE and are very similar in appearance to the incompatible element–enriched boundary layers observed by Kuehner et al. (1989; see their Fig. 2). Because the coatings follow the shapes of the irregular Fe-rich rim projections, they are similarly interpreted as quenched incompatible element–rich boundary layers.

ORIGIN OF Fe-RICH SANIDINE

The rarity of Fe-rich sanidine can be related to the unusual chemical conditions necessary for its formation. The magma must have (1) an oxidized Fe^{3+}-rich composition, (2) low Al, (3) high K, and (4) silica saturation. Such chemical features are unusual in the common magmatic rocks but are characteristic of the lamproite clan (Mitchell and Bergman 1991). These unusual, primary chemical features of sample LH37 (Table 1) were further enhanced through fractional crystallization of the earlier precipitating phases, resulting in an average residual glass composition having 28% normative quartz and 14% K_2O (Table 1); yet the glass is extremely Al deficient, as shown by the 21% normative potassium metasilicate. During precipitation of the sanidine cores, it is likely that Fe^{3+}, Ti, and Mg were preferentially partitioned into the liquid and a boundary layer rich in these elements developed.

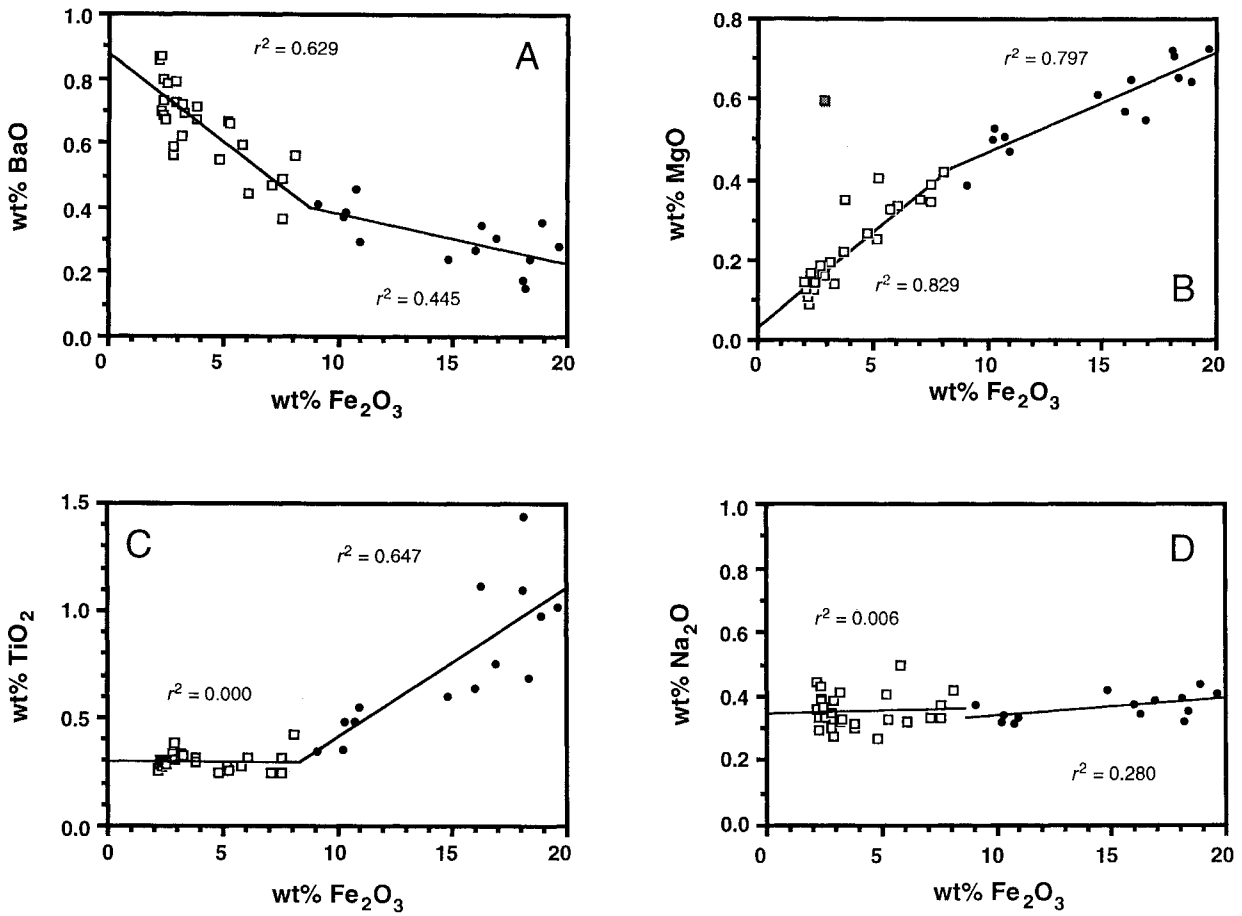

FIGURE 6. Weight-percent plots of minor element oxides vs. Fe_2O_3, displaying core-rim zoning profiles; (**A**) BaO, (**B**) MgO, (**C**) TiO_2, (**D**) Na_2O. Separation of core (squares) and rim compositions (circles) was based on analysis locations in Figure 1B. Regression lines for each group are indicated. The solid square (**B**) was excluded from the regression.

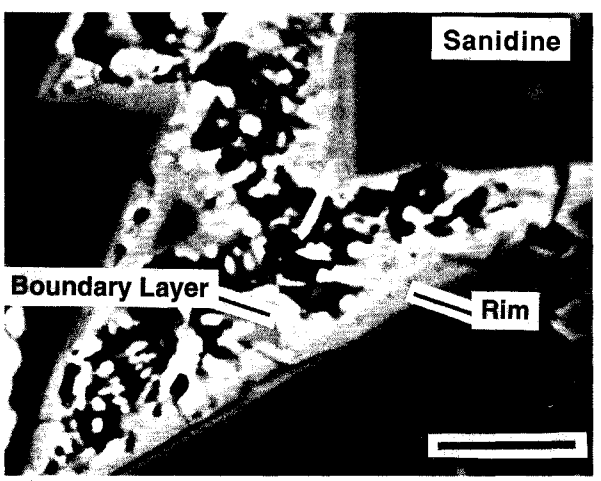

FIGURE 7. BSE image of sanidine rims and adjacent glass. The planar Fe-rich rims have ragged overgrowths, which are even more Fe-rich. The irregular surfaces of the overgrowths are coated with a bright material interpreted as quenched, incompatible element–rich, liquid boundary layers (see bottom center, and compare with Fig. 2 of Kuehner et al. 1989). Scale bar is 10 μm.

As growth of sanidine progressed at an accelerating rate during quenching, the Fe^{3+}-rich boundary-layer liquid became increasingly important in continuing to stabilize sanidine in the extremely Al-deficient perpotassic liquid through the substitution of Fe^{3+} for Al.

In both the Leucite Hills and Cancarix occurrences (Linthout and Lustenhouwer 1993), Fe-rich rims form on groundmass sanidine. Linthout and Lustenhouwer suggested that the Fe-rich rims grew during quenching of the Cancarix magma as a result of the evolution of a vapor phase, and evidence suggests that the evolution of a vapor phase may also have coincided with the formation of rims on the Leucite Hills sanidine grains. Analyses of Leucite Hills phlogopite, Ti- and K-rich richterite, and apatite show significant amounts of F (Cross 1897; Stormer and Carmichael 1971; Kuehner, unpublished data), resulting in whole-rock analyses having 0.6–0.7 wt% F (Kuehner et al. 1981). Yet F (and S) is below the detection limit (<0.04 wt%) in the microprobe analyses of the interstitial glass in sample LH37 (Table 1), suggesting that F (and S, H_2O) exsolved from residual liquids prior to or during quenching. As F, combined with H_2O, acts

to depolymerize and thus decrease the viscosity of silicate melts, the evolution of an F and H_2O vapor from the late-stage liquid would rapidly increase its viscosity (Foley et al. 1986). Such an event would slow diffusion of cations in the groundmass liquid, thus enhancing the role that the adjacent boundary-layer liquid has in controlling the rim composition of precipitating phases.

Acknowledgments

The public-domain program NIH Image was written by Wayne Rasband, U.S. National Institute of Health, and is available from the Internet by anonymous FTP from zippy.nimh.nih.gov. SAED data were collected in the interplanetary dust lab of D.E. Brownlee, following the microtome sample preparation by J.P. Bradley. CBED patterns were collected at the University of Washington Materials Analysis Laboratory with the help of G.H. Kim. Comments on an early version of the manuscript from H. Yang and B.W. Evans are much appreciated. Reviews by J. Stormer and G. Nord much improved the manuscript.

References cited

Albarede, F., and Bottinga, Y. (1972) Kinetic disequilibrium in trace element partitioning between phenocrysts and host lava. Geochimica et Cosmochimica Acta, 36, 141–156.

Annersten, H. (1976) New Mössbauer data on iron in potash feldspar. Neues Jahrbuch für Mineralogie Monatshefte, 8, 337–343.

Barton, M., and Hamilton, D.L. (1978) Water-saturated melting relations to 5 kilobars of three Leucite Hills lavas. Contributions to Mineralogy and Petrology, 66, 41–49.

——— (1982) Water-saturated melting experiments bearing upon the origin of potassium-rich magmas. Mineralogical Magazine, 45, 267–278.

Best, M.G., Henage, L.F., and Adams, J.A.S. (1968) Mica peridotite, wyomingite, and associated potassic igneous rocks in northeastern Utah. American Mineralogist, 53, 1041–1048.

Bevington, P.R. (1969) Data reduction and error analysis for the physical sciences, 336 p. McGraw-Hill, New York.

Bradley, W.H. (1964) Geology of the green river formation and associated Eocene rocks in southwest Wyoming and adjacent parts of Colorado and Utah. U.S. Geological Survey Professional Paper, 496-A, A1–A86.

Bryan, W.B. (1974) Fe-Mg relationships in sector-zoned submarine basalt plagioclase. Earth and Planetary Science Letters, 24, 157–165.

Carmichael, I.S.E. (1967) The mineralogy and petrology of the volcanic rocks from the Leucite Hills. Contributions to Mineralogy and Petrology, 15, 24–66.

Champness, P.E. (1987) Convergent beam electron diffraction. Mineralogical Magazine, 51, 33–48.

Cross, W. (1897) Igneous rocks of the Leucite Hills and Pilot Butte, Wyoming. American Journal of Science, 14, 115–141.

Emmons, S.F. (1877) Descriptive geology. In U.S. Army Engineer Department of Professional Papers, 2, 236–238.

Foley, S.F., Taylor, W.R., and Green, D.H. (1986) The effect of fluorine on phase relationships in the system $KAlSiO_4$-Mg_2SiO_4-SiO_2 at 28 kbar and the solution mechanism of fluorine in silicate melts. Contributions to Mineralogy and Petrology, 93, 46–55.

Grove, T.L., and Bence, A.E. (1977) Experimental study of pyroxene-liquid interaction in quartz-normative basalt 15597. Proceedings of the Lunar and Planetary Science Conference, 8, 1549–1579.

Gunter, W.D., Hoinkes, G., and Ogden, P. (1990) Origin of leucite-rich and sanidine-rich flow layers in the Leucite Hills volcanic field, Wyoming. Journal of Geophysical Research, 96, 15911–15928.

Gupta, A.K., and Fyfe, W.S. (1975) Leucite survival: The alteration to analcime. Canadian Mineralogist, 13, 361–363.

Kuehner, S.M., Edgar, A.D., and Arima, M. (1981) Petrogenesis of the ultrapotassic rocks from the Leucite Hills, Wyoming. American Mineralogist, 66, 663–677.

Kuehner, S.M., Laughlin, J.R., Grossman, L., Johnson, M.L., and Burnett, D.S. (1989) Determination of trace element mineral/liquid partition coefficients in melilite and diopside by ion and electron microprobe techniques. Geochimica et Cosmochimica Acta, 53, 3115–3130.

Kuehner, S.M., and Joswiak, D.J. (1993) Electron microprobe and electron diffraction study of a new ferric iron sanidine from the Leucite Hills, Wyoming. In G.W. Bailey and C.L. Rieder, Eds., Proceedings of the 51st Annual Meeting of the Microscopy Society of America, 1236 p.

Linthout, K., and Lustenhouwer, J.W. (1993) Ferrian high sanidine in a lamproite from Cancarix, Spain. Mineralogical Magazine, 57, 289–299.

Lofgren, G. (1980) Experimental studies on the dynamic crystallization of silicate melts. In R.B. Hargraves, Ed., Physics of magmatic processes, p. 487–551. Princeton University Press, New Jersey.

McDowell, F.W. (1971) K-Ar ages of igneous rocks from the western United States. Isochron West, 2, 1–16.

Mitchell, R.H., Platt, R.G., and Downey, M. (1987) Petrology of lamproites from Smokey Butte, Montana. Journal of Petrology, 28, 645–677.

Mitchell, R.H., and Bergman, S.C. (1991) Petrology of lamproites, 447 p. Plenum, New York.

Ogden, P.R. (1979) The geology, major element geochemistry, and petrogenesis of the Leucite Hills volcanic rocks, Wyoming. Ph.D. thesis, University of Wyoming, Laramie.

Petrov, I., and Hafner, S.S. (1988) Location of trace Fe^{3+} ions in sanidine, $KAlSi_3O_8$. American Mineralogist, 73, 97–104.

Reed, S.J.B. (1973) Principles of X-ray generation and quantitative analysis with the electron microprobe. In C.A. Anderson, Ed., Microprobe analysis, p. 53–81. Wiley, New York.

Roedder, E.W. (1951) The system K_2O-MgO-SiO_2, part 2. American Journal of Science, 249, 224–248.

Schairer, J.F. (1948) Phase equilibrium relationships in the quaternary system K_2O-MgO-Al_2O_3-SiO_2 (preliminary report). Geological Society of America Bulletin, 56, 1349.

Sclar, C.B., and Benimoff, A.I. (1980) Magnesium in anorthite: Synthesis and petrological significance of $CaMgSi_3O_8$ (abs.). American Geophysical Union, 61, 392.

Shimizu, N. (1983) Interface kinetics and trace element distribution between phenocrysts and magma. In S.S. Augustithis, Ed., The significance of trace elements in solving petrogenetic problems and controversies, p. 175–195. Theophrastus, Athens, Greece.

Smith, J.V. (1974) Feldspar minerals: 2. Chemical and textural properties, 690 p. Springer-Verlag, Berlin.

Smith, J.V., and Brown, W.L. (1988) Feldspar minerals: 1. Crystal structures, physical, chemical, and microtextural properties, 828 p. Springer-Verlag, Berlin.

Smith, M.P., and Franks, P.C. (1986) Mg-rich hollow sanidine in partially melted granite xenoliths in a mica peridotite at Rose dome, Woodson County, Kansas. American Mineralogist, 71, 60–67.

Stormer, J.C., and Carmichael, I.S.E. (1971) Fluorine-hydroxyl exchange in apatite and biotite: A potential igneous geothermometer. Contributions to Mineralogy and Petrology, 31, 121–131.

Tsuchiyama, A. (1985) Crystallization kinetics in the system $CaMgSi_2O_6$-$CaAl_2Si_2O_8$: Development of zoning and kinetics effects on element partitioning. American Mineralogist, 70, 474–486.

Woensdregt, C.F. (1983) Structural morphology of high sanidine ($KAlSi_3O_8$). Zeitschrift für Kristallographie, 162, 239–255.

Wones, D.R., and Appleman, D.E. (1961) X-ray crystallography and optical properties of synthetic monoclinic $KFeSi_3O_8$ iron-sanidine. U.S. Geological Survey Professional Paper, 424C, C309–C310.

Yagi, K., and Matsumoto, H. (1966) Note on the leucite-bearing rocks from the Leucite Hills, Wyo., U.S.A. Journal of the Faculty of Science, Hokkaido University, series IV, Geology and Mineralogy, 13, 301–312.

Manuscript received October 18, 1994
Manuscript accepted September 15, 1995